Development of Fine-Resolution Analyses and Expanded Large-Scale Forcing Properties. Part II: Scale-Awareness and Application to Single-Column Model Experiments

Sha Feng[1,2*], Zhijin Li[2,1], Yangang Liu[3], Wuyin Lin[3], Minghua Zhang[4], Tami Toto[3], Andrew M. Vogelmann[3], and Satoshi Endo[3]

1. Joint Institute for Regional Earth System Science and Engineering, University of California at Los Angeles, Los Angeles, CA 90095

2. Jet Propulsion Laboratory, California Institute of Technology, Pasadena, CA 91109

3. Environmental Sciences Department, Brookhaven National Laboratory, Upton, NY 11973

4. Stony Brook University, Stony Brook, NY 11794

Submitted to Journal of Geophysical Research – Atmosphere (special issue), June 2014

Revised: December 2014

**Corresponding author:* Sha Feng

[1]University of California at Los Angeles

Joint Institute for Regional Earth System Science and Engineering

Los Angeles, CA 90095

Email: sfeng@jifresse.ucla.edu

[2]Jet Propulsion Laboratory

M/S 300-323

4800 Oak Grove Drive,

Pasadena, CA 91109

Email: Sha.Feng@jpl.nasa.gov

Abstract

Fine-resolution three-dimensional fields have been produced using the Community Gridpoint Statistical Interpolation (GSI) data assimilation system for the U.S. Department of Energy's Atmospheric Radiation Measurement (ARM) Southern Great Plains (SGP) region. The GSI system is implemented in a multi-scale data assimilation framework using the Weather Research and Forecasting (WRF) model at a cloud-resolving resolution of 2 km. From the fine-resolution three-dimensional fields, large-scale forcing is derived explicitly at grid-scale resolution; a subgrid-scale dynamic component is derived separately, representing subgrid-scale horizontal dynamic processes. Analyses show that the subgrid-scale dynamic component is often a major component over the large-scale forcing for grid scales larger than 200 km. The single-column model (SCM) of the Community Atmospheric Model version 5 (CAM5) is used to examine the impact of the grid scale and subgrid-scale dynamic components on simulated precipitation and cloud fields associated with a meso-scale convection system. It is found that grid-scale size impacts simulated precipitation, resulting in an overestimation for grid scales of about 200 km but an underestimation for smaller grids. The subgrid-scale dynamic component has an appreciable impact on the simulations, suggesting that grid scale and subgrid-scale dynamic components should be considered in the interpretation of SCM simulations.

1. **Introduction**

In Part I [*Li, et al.,* 2014], the first in a series of three papers, data assimilation is used to produce fine-resolution three-dimensional fields of meteorological and other variables for the U.S. Department of Energy's Atmospheric Radiation Measurement (ARM) Southern Great Plains (SGP) site. The Community Gridpoint Statistical Interpolation (GSI) data assimilation system is implemented in a multi-scale data assimilation (MS-DA) algorithm to manage the difficulties that arise when operating at fine-resolution. The GSI system is an operational data assimilation system developed by the National Centers for Environmental Prediction (NCEP). The Weather Research and Forecasting (WRF) model is used and configured at a cloud-resolving resolution of 2 km [*Randall et al.*, 2003].

The ARM program established the SGP site in 1992, and has continuously gathered a wide variety of observations since then. The ARM SGP site encompasses the area of a typical global climate model (GCM) grid cell and contains high-resolution surface-based measurements focused on cloud-related fast processes [*Stokes and Schwartz*, 1994; *Ackerman and Stokes*, 2003; *Mather and Voyles*, 2013]. The MS-DA algorithm assimilates ARM measurements along with observations processed by NCEP, particularly radiances from an array of polar orbiting satellites. The fine-resolution three-dimensional fields generated by the MS-DA were evaluated in Part I and found to be capable of reproducing a meso-scale convective system with its associated clouds and precipitation.

Large-scale forcing has been routinely produced for the SGP site for a variety of applications [e.g., *Xie et al*., 2004], the most important of which is to drive single-column models (SCMs) for testing physical parameterizations in GCMs. The MS-DA analysis is used to expand the properties of large-scale forcing to include scale-awareness and hydrometeor forcing. In Part

III [*S. Feng, Z. Li, W. Lin, Y. Liu, M. Zhang, T. Toto, A. M. Vogelmann, and S. Endo*, Development of fine-resolution analyses and expanded properties of large-scale forcing. Part III: Hydrometeor forcing and application to single-column model experiments, submitted to *J. Geophys. Res.*, 2014], we demonstrate the significant impact of hydrometeor forcing on SCM simulations as did *Petch and Dudhia* [1998]; yet so far hydrometeor forcing is not part of existing large-scale forcing products. This paper focuses on characterizing the scale-aware forcing and assesses its impact on SCM simulations.

Here 'scale-aware properties' of the large-scale forcing refers to its explicit grid-scale dependence and subgrid-scale dynamic component. The grid-scale dependence has become important to address as GCM grid spacing size, or spatial resolution, has become increasingly fine. The spatial resolutions of current GCMs range from an order of 100 km to an order of 10 km [*IPCC*, 2013]. The large-scale forcing used to drive an SCM must represent the grid-scale associated with the GCM, noting that a given GCM can operate at a range of spatial resolutions rather than having a fixed resolution. As we will show in section 3, large-scale forcing fields vary significantly with grid scale and, correspondingly, SCM simulations are sensitive to these variations. Thus, the dependence of large-scale forcing on grid scale must be considered when interpreting SCM simulations.

Generally, the subgrid-scale dynamic component consists of the subgrid-scale vertical flux divergences and horizontal flux divergences that are not parameterized. The non-parameterized component must be included as part of the large-scale forcing, as we will see in section 2. In the latest GCMs, the subgrid-scale vertical fluxes associated with turbulence and convection are parameterized; so we may assume that the significant subgrid-scale vertical fluxes are accounted for in the parameterization. The subgrid-scale horizontal fluxes are also

parameterized in GCMs, but only partially. Subgrid-scale horizontal fluxes are non-linear processes that act on the atmospheric flow system via downscale and upscale interactions. Downscale interactions are parameterized by hyper-diffusion ($\sim\nabla^{2h}$). It has been proposed that upscale interactions be parameterized as stochastic forcing, to account for the irregular and unpredictable nature of subgrid-scale dynamic processes [e.g., Palmer, 2001; Hoskins et al., 2004]. Stochastic parameterizations are included in some numerical weather prediction models [Buizza et al., 1999; Shutts, 2001], but they are not yet implemented in most GCMs. Thus, it is necessary to include the subgrid-scale horizontal flux divergence in the large-scale forcing.

In existing large-scale forcing products, the subgrid-scale horizontal flux component is often implicitly included. The standard ARM large-scale forcing generated using the constrained objective variational analysis [*Zhang and Lin*, 1997] implicitly includes it, although it could be underestimated due to the limited number of grid points used for the line integration to calculate the area-mean flux divergence [*Ooyama*, 1987]. The large-scale forcing derived from cloud-resolving model simulations by *Bechtold et al.* [2000] contained the subgrid-scale component as well. We will show that it can be a significant component in large-scale forcing and appreciably impact SCM simulations.

The paper is organized as follows. Section 2 describes the formulation for deriving large-scale forcing and the subgrid-scale dynamic component. Section 3 presents derived large-scale forcings for different grid scales to examine the scale dependence. Section 4 presents the subgrid-scale dynamic component and quantifies its importance in relation to grid-scale forcing. In section 5, we conduct experiments, using the single-column version of the Community Atmospheric Model version 5 (CAM5), known as SCAM5, to demonstrate the sensitivity of

SCM simulations to grid-scale size and to the subgrid-scale dynamic component. A summary and discussion are given in section 6.

2. Scale-aware large-scale forcing

Following Part I [*Li, et al.*, 2014], the thermodynamic and moisture conservation equation for an SCM can be written in the form,

$$\frac{\partial \bar{T}}{\partial t} = \left(\frac{\partial \bar{T}}{\partial t}\right)_{LS} - \overline{\nabla \cdot V'T'} - \frac{1}{\gamma_T}\left(\bar{T} - \bar{T}_{LS}\right) + \frac{\overline{Q}}{c_p} - \left(\frac{\overline{\partial \omega' T'}}{\partial p} - \frac{\overline{\omega' \alpha'}}{c_p}\right), \quad (1)$$

$$\frac{\partial \bar{q}}{\partial t} = \left(\frac{\partial \bar{q}}{\partial t}\right)_{LS} - \overline{\nabla \cdot V'q'} - \frac{1}{\gamma_\tau}\left(\bar{q} - \bar{q}_{LS}\right) + \bar{S} - \frac{\partial \overline{\omega' q'}}{\partial p}, \quad (2)$$

where,

$$\left(\frac{\partial \bar{T}}{\partial t}\right)_{LS} = -\bar{V} \cdot \nabla \bar{T} - \bar{\omega}\left(\frac{\partial \bar{T}}{\partial p} - \frac{\bar{\alpha}}{c_p}\right), \quad (3)$$

$$\left(\frac{\partial \bar{q}}{\partial t}\right)_{LS} = -\bar{V} \cdot \nabla \bar{q} - \bar{\omega}\frac{\partial \bar{q}}{\partial p}. \quad (4)$$

The variables are defined as follows: V, horizontal wind; ω, vertical p-velocity; p, pressure; p_0, surface pressure; α, specific volume of the air; c_p, the specific heat at constant volume; ∇, the horizontal del operator; Q, the heating rate; S, the source of water vapor; and γ_τ, the relaxation time scale. The overbar denotes a horizontal average over a given domain. The second term on the right-hand side in Eqs. (1) and (2) is the subgrid-scale dynamic component; the third represents the relaxation term. Relaxation is linked to the horizontal advection term and in turn is linked to subgrid-scale dynamic term [*Randall and Cripe, 1999*]. This linkage implies that the subgrid-scale dynamic component and relaxation terms may be

dynamically inappropriate to include together in Eqs. (1) and (2). We will further address this topic in section 5.3.

Using domain averages, we can calculate the grid-scale component of each T forcing and q forcing as defined by Eqs. (3) and (4), respectively. For simplicity, we call the grid-scale forcing of Eq. (3) the T forcing and the grid-scale forcing of Eq. (4) the q forcing. Here the subgrid-scale dynamic component is the subgrid-scale horizontal flux only.

The subgrid-scale horizontal and vertical fluxes are not independent but, rather, are related to each other through the continuity equation. The vertical flux consists of a component that is parameterized and a component that is not. Since the primary component of the vertical flux has been parameterized, the subgrid-scale horizontal flux in the large-scale forcing must be included to keep consistency between the subgrid-scale horizontal and vertical fluxes.

3. Grid-scale forcing

SCMs have been used to test and evaluate physical parameterization schemes as early as two decades ago [e.g., *Betts and Miller*, 1986]. Since then, GCM resolutions have become increasingly fine, from a few 100 km down to tens of km. The ARM SGP site was initially designed to match the grid scale of GCMs from the late 80s and early 90s, covering a domain about 300 km in diameter for which the ARM large-scale forcing product was produced. The observing area for the ARM SGP site has been reduced recently, focusing on a smaller domain comparable to the finer spatial resolutions used in newer GCMs.

The MS-DA analysis offers the flexibility of deriving grid-scale forcing fields for a range of grid sizes. We calculate the grid-scale forcing for grid scales of 300, 200, 100, and 50 km (Figure 1); the domains are, respectively, D300, D200, D100, and D50. By definition, the

153 subgrid-scale dynamic component is the deviation from the domain average, and hence it is
154 straightforward to calculate the subgrid-scale dynamic component for all domains.
155 Figure 1 depicts the development of a major precipitation band during a meso-scale
156 convective system (MCS) [*Houze*, 2004] that occurred from 13 to 15 June 2007. Figure 2
157 illustrates the differences in large-scale forcing fields associated with the four grid scales. As
158 expected, the vertical velocity, and the grid-scale T and q forcings increase in terms of temporal
159 variability and intensity as spatial resolution increases. The variability of the grid-scale forcing is
160 associated with the intensification, decay and movement of the MCS. These features are
161 discussed further in section 4.
162
163 **4. Subgrid-scale dynamic component**
164 This section characterizes the subgrid-scale dynamic component during the MCS event.
165 Figure 3 displays the temperature subgrid-scale dynamic component (SS), the grid-scale
166 component (LS), and the combined amount (LS+SS) for the four grid scales. The subgrid-scale
167 dynamic component (Figures 3a1-3a4) tends to have large intensities that are primarily confined
168 to the boundary layer. For D100, we also see significant values near 700 hPa around 06 UTC 14
169 June. There is strong temporal variability, which can be attributed to the related meso-scale
170 activity. A maximum occurs around 06 UTC 14 June, when the MCS reaches its peak intensity
171 between 03 UTC and 09 UTC 14 June. Overall, the magnitude of the subgrid-scale dynamic
172 component gets larger for smaller grid scales.
173 To show the significance of the subgrid-scale dynamic component, we compare it with
174 the corresponding grid-scale horizontal advection, which does not include the subgrid-scale
175 component (Figures 3b1-3b4). For the D300 and D200 domains and in the lower troposphere,

176 the subgrid-scale dynamic component is comparable to the grid-scale counterpart. For the D100
177 and D50, the overall magnitude of the subgrid-scale component is generally smaller than its the
178 grid-scale counterpart, but its magnitude is larger during the intensive convective time period at
179 approximately 06 UTC 14 June.

180 Figure 4 (a1-a4) displays the subgrid-scale dynamic component of q forcing for the four
181 grid scales. Similar to the subgrid-scale dynamic component of T forcing, the temporal
182 variability in the q subgrid-scale dynamic component is also concentrated in the lower
183 troposphere and peaks around 06 UTC 14 June. We note that for the smallest grid, D50, the
184 subgrid-scale component tends to have a smaller magnitude. We expect that the importance of
185 the subgrid-scale dynamic component would be further reduced as grid resolution increases. This
186 is consistent with the experience that an increase in GCM resolution generally improves model
187 performance.

188 To illustrate the relative significance of the subgrid-scale dynamic component, we
189 compare the subgrid-scale dynamic components in Figures 3 and 4 to the total grid-scale forcing
190 in Figure 2. Near the surface or even in the lower troposphere, the subgrid-scale dynamic
191 component could be close to 100 % of the magnitude of the total T forcing and q forcing for
192 D300, ~60 % and ~90 % for D200, ~25 % and 50 % for D100, and ~20 % of both for D50,
193 respectively. Thus, the subgrid-scale dynamic component can be a significant component of the
194 total large-scale forcing fields and fundamentally impact SCM simulations as will be shown in
195 the next section.

196

197 **5. Single-column model sensitivity experiments**

198 Here we examine the sensitivity of SCM simulations to grid scale and subgrid-scale

dynamic components, and their relative significance to each other. The SCM experiments are conducted using SCAM5. SCAM5 contains all physical processes used in CAM5 [*Neale et al.*, 2012], which includes the cloud microphysics and macrophysics schemes. Details about microphysical conversions among cloud liquid droplets, ice crystal, rain and snow can be found in *Gettelman et al.* [2008], *Morrison and Gettelman* [2008], *Gettelman et al.* [2010], and *Song et al.* [2013].

To quantify the sensitivity of SCAM5 simulations to the subgrid-scale dynamic component, four experiments are conducted for each of the four grid scales (D300, D200, D100 and D50). These experiments are summarized in Table 1 and are conducted with and without relaxation. When analyzing the experiments, we focus primarily on the sensitivity of simulated precipitation and cloud fraction to the grid scale and to the subgrid-scale dynamic components. The simulated precipitation and cloud fraction are compared to observations. The precipitation data are from the ABRFC (Arkansas-Red Basin River Forecast Center, available at http://www.arm.gov/data/vaps/abrfc). The data consist of 4-km hourly precipitation estimates from a combination of WSR-88D Next Generation Radar (NEXRAD) precipitation estimates and rain gauge reports. We use hourly cloud fractional occurrence over the ARM SGP Central Facility from the Active Remote Sensing of Clouds (ARSCL) [*Clothiaux et al.*, 2000; *Clothiaux et al.*, 2001], which is determined from measurements made by the Millimeter Wavelength Cloud Radar (MMCR) and Micropulse Lidar (MPL) and is as provided in the ARM Best Estimate Data Products (ARMBE) [*Xie et al.*, 2010]. Note that observations used in the evaluation were not assimilated in the MS-DA analysis.

5.1. Derived forcing for different grid scales

222 Figure 5 presents domain-averaged simulated precipitation rate from the SCAM5
223 experiments, the MS-DA analysis, and the domain-averaged precipitation rate from observations.
224 Before discussing the SCAM5 results, we look at the precipitation from the MS-DA. For all four
225 grid scales, the MS-DA realistically reproduces the timing of the main convective precipitation
226 event; the magnitude is realistically represented at D300 but overestimated for the other domains.
227 Given that ABRFC precipitation is not assimilated to the MS-DA system, the realistic timing of
228 the simulated MS-DA precipitation occurs as the result of proper internal balances in the MS-DA
229 analysis.
230 We first compare the MS-DA and SCAM5 simulated precipitation. For the case of
231 LS_norelax (dashed blue), where the grid-scale forcing component is used without relaxation,
232 the precipitation rates are comparable to observations for the D300 grid scale, are overestimated
233 for D200, and are underestimated for D100 and D50. In fact, the largest precipitation event does
234 not even occur for D50. The parameterization in SCAM5 seems best suited for 300-km grid scale,
235 highlighting the importance of the scale-dependence of large-scale forcing. For the case of
236 LS_3hrelax (dashed red), there is a clear reduction of precipitation rate during the convective
237 period for D300 and D200 compared to LS_norealx.
238 For the case of LS+SS_norelax (solid blue), where the grid-scale and subgrid-scale
239 dynamic components are both used and no relaxation is applied, the precipitation rates are
240 underestimated for most domains except D200. For the case of LS+SS_3hrelax (solid red), as for
241 the LS cases, the precipitation rate is reduced for D300 when relaxation is applied. Relaxation
242 tends to reduce the precipitation rate for the 300- and 200-km grid scales. For the smaller grid
243 scales of 100 and 50 km, the impact of the relaxation is not clear.

A synthesis of the results from all four cases points to a tendency of the SCAM5 to underestimate precipitation rate more so as grid resolution increases below 200 km (i.e., as grid size decreases). This tendency might be associated with the MCS structure and its processes so should not be viewed as a general conclusion. However, the results suggest that the sensitivity of the SCM simulation to grid size must be taken into account when attributing simulation errors to physical parameterization schemes.

Since the clouds simulated by SCMs are often sensitive to forcing [e.g., *Fridlind et al.*, 2012], we compare the performance of cloud simulations without relaxation applied to observations. Figure 6 shows the ARMBE cloud fraction during the time period for the SCM simulations. Two convective events corresponding strong precipitation rate can be seen during 09 UTC to 15 UTC 13 June and 03 UTC to 12 UTC 14 June. We note that the observed cloud fractions are derived from profiles of point observations, while the SCAM5 cloud fraction represents the average over a domain of a given grid size. Although a meaningful comparison between SCAM5 results with observations usually requires a sufficiently long observation period of the latter, the general characteristics of a large-scale phenomenon such as an MCS can be captured.

In Figure 7, we see that high clouds are overestimated for grid-scales D300 and D200 (both of Exps. LS and LS+SS), but that this overestimation is significantly reduced for the smaller grid scales D100 and D50. This reduction of cloud fraction at higher altitudes is most evident around 21 UTC 13 June. The observations show few high clouds during a period of about 6 hours, from 18 UTC 13 June to 00 UTC 14 June. We conclude that the SCAM5 overestimates high clouds for all grid scales but that the overestimation is not significant for the small grid scales D100 and D50.

The SCAM5 simulations underestimate the lower-level cloud fractions for all grid scales. For grid scales D100 and D50, in particular, cloud fraction does not extend to lower levels during the main precipitation event that occurs from 03 UTC to 12 UTC 14 June. It is clear from Figure 5 that the simulated precipitation is less than 1/3 of that observed, which could be related to vertical velocity. In Figure 2 (a1-a4), the upward vertical velocities are associated with the main precipitation event for D300 and D200, but strong downward vertical velocities--as large as 0.3 m/s--occur in the lower troposphere for D100 and D50. It is unlikely that this strong downward vertical velocity is caused by the MS-DA system because it can simulate the precipitation rates well (Figure 5, gray lines), which suggests that its vertical velocities are reasonable. Therefore, the SCAM5 may be limited when dealing with strong vertical velocities associated with small grid scales such as D100 and D50.

5.2. Impact of the subgrid-scale dynamic component

The impact of the subgrid-scale dynamic component can be determined from the differences between the experiments that consider only the grid-scale component (Exps. LS) and those that use the grid-scale and subgrid-scale dynamic components (Exps. LS+SS). In Figure 5, we see that the subgrid-scale dynamic component reduces the precipitation rates for D300 but not for the grid scales smaller than 200 km. In terms of cloud fraction, the subgrid-scale dynamic component tends to increase mid- and low-level cloud fraction but reduce high-level cloud fraction for D300 and D200 (Figure 7), while it decrease mid- and low-level cloud fraction but increase high-level clouds for D100, For D50, the impact is minor.

5.3. Subgrid-scale dynamic component vs. relaxation

290 The relaxation terms in Eqs. (1 and 2) have often been used in SCM simulations, but they
291 are not independent of the subgrid-scale dynamic component as we pointed out in section 2.
292 *Ghan et al.* [2000] showed that the impact of relaxation on SCM simulations tends to be mixed,
293 either improving or degrading the SCM performance; thus, the role of the relaxation term needs
294 to be further quantified. Since we have determined the subgrid-scale dynamic component, a
295 direct comparison can be made between the impacts of relaxation and the subgrid-scale dynamic
296 component.
297 Relaxation reduces precipitation rate for D300 and D200, as can be seen in Figure 5 by
298 the difference between Exps. LS_norelax and LS_3hrelax and between LS+SS_norelax and
299 LS+SS_3hrelax. The precipitation rate is halved during the main precipitation event on 14 June
300 for D300. In section 5.2, we saw that the subgrid-scale dynamic component reduces
301 precipitation as well, as can be seen from the difference between Exps. LS_norelax and
302 LS+SS_norelax. For D300, the precipitation in Exps. LS_3hrelax and LS+SS_norelax are
303 reduced by similar amount of ~1.0 mm/hr compared to Exp. LS_norelax during the convective
304 event. This result seems to suggest that, in terms of precipitation, relaxation may play a role
305 similar to the subgrid-scale dynamic component. We note that for the case of LS+SS_3hrelax,
306 where the subgrid-scale dynamic component and 3-hr relaxation are applied, the precipitation
307 rate largely drifts apart from the observation for D300, but this drift is not seen at the smaller
308 grid scales. One should be cautions of using relaxation when the subgrid-scale dynamic
309 component is included.
310 For the cloud simulation, the impact of relaxation tells a different story. Subgrid-scale
311 dynamics, without relaxation, often increases mid- and low-level cloud fraction (Figure 7),
312 whereas relaxation tends to reduce mid- and low-level cloud fractions (compare Figure 8 to

313 Figure 7). The impact of relaxation on cloud formation must be different from the mechanism
314 responsible for precipitation reduction.

315 It is beyond the scope of this paper to attribute the precipitation reduction to specific
316 microphysical processes; however we hypothesize that the precipitation reduction caused by
317 relaxation is related to the reduction of mid- and low-level clouds. Given that the impact on mid-
318 and low-level clouds is opposite to the subgrid-scale dynamic component, caution should be
319 exercised when using the subgrid-scale dynamic component with relaxation in SCMs.

320

321 **6. Summary and Discussion**

322 We have addressed scale-aware large-scale forcing, which refers to the large-scale
323 forcing associated explicitly with grid-scale and subgrid-scale components. The grid-scale
324 component of the forcing aims to account for the wide range of spatial resolutions of current
325 GCMs, from an order of 100 km to finer resolutions of an order of 10 km [*IPCC*, 2013]. The
326 grid-scale and subgrid-scale dynamic components are derived based on a multi-scale data
327 assimilation system with WRF at a cloud-resolving resolution of 2 km, which was applied to the
328 ARM SGP region. Comprehensive SCAM5 experiments are conducted to examine the
329 dependence on grid scale and sensitivity to the subgrid-scale dynamic component in terms of
330 simulated precipitation and cloud fraction.

331 As expected, the large-scale forcing intensity and temporal variability increase as spatial
332 scales are reduced. The increase is most pronounced during the MCS precipitation events. The
333 SCAM5-simulated precipitation is overestimated for scales of about 200 km and reverses to be
334 underestimated for smaller scales. The results indicate that spatial scale needs to be considered in
335 the interpretation of SCM simulations.

The analyses show that the subgrid-scale dynamic component, the subgrid-scale flux divergence due to subgrid-scale dynamic processes, often provide significant horizontal advection for spatial scales larger than 200 km and is a non-negligible component of the large-scale forcing. The subgrid-scale dynamic component has a beneficial impact on the SCAM5 simulations, especially for larger domains. Such results support our argument that the subgrid-scale dynamic processes are partially parameterized as hyper-diffusion in CAM5, and thus its inclusion enhances the consistency between the horizontal flux divergence and the vertical flux divergence that is accounted for in parameterizations.

The subgrid-scale dynamic component and relaxation are dynamically related [*Randall and Cripe*, 1999]. The impacts of the subgrid-scale dynamic component and relaxation in the SCAM5 are similar in terms of precipitation rate but not cloud fraction. This result agrees with the conclusion in *Ghan et al.* [2000] that the impact of relaxation may vary for different field variables.

We have shown that the subgrid-scale dynamic component is a significant component in large-scale forcing fields, and that SCM simulations are sensitive to it. However, from the experiments presented, we cannot reach the conclusion that the inclusion of subgrid-scale dynamic component improves the SCM simulation from the experiments that are presented. This is because the SCM responds to the subgrid-scale dynamic component in a complex way.

Acknowledgements. The research described in this publication was supported by the U.S. Department of Energy Earth System Modeling (ESM) program via the FASTER project (http://www.bnl.gov/faster). This research was carried out, in part, at the Jet Propulsion Laboratory (JPL), California Institute of Technology, under a contract with the National

359 Aeronautics and Space Administration (NASA). The authors are grateful to Drs. Ann Fridlind
360 (NASA Goddard Institute for Space Studies) and Leo J. Donner (Geophysical Fluid Dynamics
361 Laboratory) for stimulating discussions and insightful suggestions. Data from the U.S.
362 Department of Energy's SGP ARM Climate Research Facility (http://www.arm.gov/) are used in
363 this article. The authors thank the anonymous reviewers for comments that were very helpful in
364 improving the manuscript.
365

References:

Ackerman, T. P., and G. M. Stokes (2003), The Atmospheric Radiation Measurement program, *Physics Today*, *56*(1), 38-44.

Bechtold, P., J. L. Redelsperger, I. Beau, M. Blackburn, S. Brinkop, J. Y. Grandper, A. Grant, D. Gregory, F. Guichard, C. How, and E. Ioannidou (2000), A GCSS model intercomparison for a tropical squall line observed during toga-coare. II: Intercomparison of single-column models and a cloud-resolving model, *Q. J. R. Meteorol. Soc.*, *126*(564), 865-888.

Betts, A. K., and M. J. Miller (1986), A new convective adjustment scheme. Part II: Single column tests using GATE wave, BOMEX, ATEX and arctic air-mass data sets, *Q. J. R. Meteorol. Soc.*, *112*(473), 693-709.

Buizza, R., M. Milleer, and T. N. Palmer (1999), Stochastic representation of model uncertainties in the ECMWF ensemble prediction system, *Q. J. R. Meteorol. Soc.*, *125*(560), 2887-2908.

Clothiaux, E. E., T. P. Ackerman, G. G. Mace, K. P. Moran, R. T. Marchand, M. A. Miller, and B. E. Martner (2000), Objective Determination of Cloud Heights and Radar Reflectivities Using a Combination of Active Remote Sensors at the ARM CART Sites, *J. Appl. Meteorol.*, *39*(5), 645-665.

Clothiaux, E. E., M. A. Miller, R. C. Perez, D. D. Turner, K. P. Moran, B. E. Martner, T. P. Ackerman, G. G. Mace, R. T. Marchand, K. B. Widener, D. J. Rodriguez, T. Uttal, J. H. Mather, C. Flynn, K. L. Gaustad, and B. Ermold (2001), The ARM Millimeter Wave Cloud Radars (MMCRs) and the Active Remote Sensing of Clouds (ARSCL) Value Added Product (VAP), *DOE Tech. Memo. ARM VAP-002.1, U.S. Department of Energy, Washington, D.C.*

389 Fridlind, A. M., A. S. Ackerman, J. P. Chaboureau, J. Fan, W. W. Grabowski, A. A. Hill, T. R.
390 Jones, M. M. Khaiyer, G. Liu, P. Minnis, H. Morrison, L. Nguyen, S. Park, J. C. Petch, J.
391 P. Pinty, C. Schumacher, B. J. Shipway, A. C. Varble, X. Wu, S. Xie, and M. Zhang
392 (2012), A comparison of TWP-ICE observational data with cloud-resolving model
393 results, *J. Geophys. Res.*, *117*(D5), D05204.
394 Gettelman, A., H. Morrison, and S. J. Ghan (2008), A New Two-Moment Bulk Stratiform Cloud
395 Microphysics Scheme in the Community Atmosphere Model, Version 3 (CAM3). Part II:
396 Single-Column and Global Results, *J. Climate*, *21*(15), 3660-3679.
397 Gettelman, A., X. Liu, S. J. Ghan, H. Morrison, S. Park, A. J. Conley, S. A. Klein, J. Boyle, D.
398 L. Mitchell, and J.-L. F. Li (2010), Global simulations of ice nucleation and ice
399 supersaturation with an improved cloud scheme in the Community Atmosphere Model,
400 *Journal of Geophysical Research: Atmospheres*, *115*(D18), D18216.
401 Ghan, S., D. Randall, K.-M. Xu, R. Cederwall, D. Cripe, J. Hack, S. Iacobellis, S. Klein, S.
402 Krueger, U. Lohmann, J. Pedretti, A. Robock, L. Rotstayn, R. Somerville, G. Stenchikov,
403 Y. Sud, G. Walker, S. Xie, J. Yio, and M. Zhang (2000), A comparison of single column
404 model simulations of summertime midlatitude continental convection, *J. Geophys. Res.*,
405 *105*(D2), 2091-2124.
406 Hoskins, B., T. N. Palmer, and G. Shutts (2004), Stochastic physics. European Centre for
407 Medium-Range Weather Forecasts,
408 http://www.ecmwf.int/about/special_projects/hoskins_stochastic_physica/report_2005.pd
409 f.
410 Houze, R. A. (2004), Mesoscale convective systems, *Rev. Geophys.*, *42*(4),
411 10.1029/2004RG000150.

IPCC (2013), *Climate Change 2013: The physical science basis. Contribution of working group I to the fifth assessment report of the intergovernmental panel on climate change*, 1535 pp.

Li, Z., S. Feng, Y. Liu, W. Lin, M. Zhang, T. Toto, A. M. Vogelmann, and S. Endo (2014), Development of Fine-Resolution Analyses and Expanded Large-Scale Forcing Properties. Part I: methodology and evaluation, *J. Geophys. Res.*, doi: 10.1002/2014JD022245.

Mather, J. H., and J. W. Voyles (2013), The Arm Climate Research Facility: A Review of Structure and Capabilities, *Bull. Amer. Meteor. Soc.*, 94, 377–392.

Morrison, H., and A. Gettelman (2008), A New Two-Moment Bulk Stratiform Cloud Microphysics Scheme in the Community Atmosphere Model, Version 3 (CAM3). Part I: Description and Numerical Tests, *J. Climate*, *21*(15), 3642-3659.

Neale, R. B., A. Gettelman, S. Park, C.-C. Chen, P. H. Lauritzen, D. L. Williamson, A. J. Conley, D. Kinnison, D. Marsh, A. K. Smith, F. Vitt, R. Garcia, J.-F. Lamarque, M. Mills, S. Tilmes, H. Morrison, P. Cameron-Smith, W. D. Collins, M. J. Iacono, R. C. Easter, X. Liu, S. J. Ghan, P. J. Rasch, and M. A. Taylor (2012), Description of the NCAR Community Atmosphere Model (CAM 5.0), *Technical Note NCAR/TN-486+STR*.

Ooyama, K. V. (1987), Scale-Controlled Objective Analysis, *Mon. Weather Rev.*, *115*(10), 2479-2506.

Palmer, T. N. (2001), A nonlinear dynamical perspective on model error: A proposal for non-local stochastic-dynamic parametrization in weather and climate prediction models, *Q. J. R. Meteorol. Soc.*, *127*(572), 279-304.

434 Petch, J. C., and J. Dudhia (1998), The Importance of the Horizontal Advection of Hydrometeors
435 in a Single-Column Model, *J. Climate*, *11*(9), 2437-2452.
436 Randall, D., and D. Cripe (1999), Alternative methods for specification of observed forcing in
437 single-column models and cloud system models, *J. Geophys. Res.*, *104*(D20), 24527-
438 24545.
439 Randall, D., S. Krueger, C. Bretherton, J. Curry, P. Duynkerke, M. Moncrieff, B. Ryan, D. Starr,
440 M. Miller, W. Rossow, G. Tselioudis, and B. Wielicki (2003), Confronting Models with
441 Data: The GEWEX Cloud Systems Study, *Bull. Am. Meteorol. Soc.*, *84*(4), 455-469.
442 Shutts, G. (2001), 'Some interpretations of stochastic physical parameterizations.' in *ECMWF*
443 *Proceedings: Key issues n the parameterization of subgrid physical processes 3-7*
444 *September 2001*, edited, pp. 111-126, European Centre for Medium-Range Weather
445 Forecasts.
446 Song, H., W. Lin, Y. Lin, A. B. Wolf, R. Neggers, L. J. Donner, A. D. Del Genio, and Y. Liu
447 (2013), Evaluation of Precipitation Simulated by Seven SCMs against the ARM
448 Observations at the SGP Site, *J. Climate*, *26*(15), 5467-5492.
449 Stokes, G. M., and S. E. Schwartz (1994), The Atmospheric Radiation Measurement (ARM)
450 Program: Programmatic Background and Design of the Cloud and Radiation Test Bed,
451 *Bull. Am. Meteorol. Soc.*, *75*(7), 1201-1221.
452 Xie, S., R. T. Cederwall, and M. Zhang (2004), Developing long-term single-column
453 model/cloud system-resolving model forcing data using numerical weather prediction
454 products constrained by surface and top of the atmosphere observations, *J. Geophys. Res.*,
455 *109*(D1), D01104.

456 Xie, S., R. B. McCoy, S. A. Klein, R. T. Cederwall, W. J. Wiscombe, M. P. Jensen, K. L.
457 Johnson, E. E. Clothiaux, K. L. Gaustad, C. N. Long, J. H. Mather, S. A. McFarlane, Y.
458 Shi, J.-C. Golaz, Y. Lin, S. D. Hall, R. A. McCord, G. Palanisamy, and D. D. Turner
459 (2010), CLOUDS AND MORE: ARM Climate Modeling Best Estimate Data, *Bull. Am.*
460 *Meteorol. Soc.*, *91*(1), 13-20.
461 Zhang, M. H., and J. L. Lin (1997), Constrained Variational Analysis of Sounding Data Based on
462 Column-Integrated Budgets of Mass, Heat, Moisture, and Momentum: Approach and
463 Application to ARM Measurements, *J. Atmos. Sci.*, *54*(11), 1503-1524.

Figure captions:

Figure 1. The domains used to calculate forcing components. The colored squares denote the following domains: 300 km × 300 km (black), 200 km × 200 km (blue), 100 km × 100 km (red), and 50 km × 50 km (green). All domains are centered on the ARM SGP central facility (36.63°N, 97.49°W). The color-filled contours show the distribution of surface precipitation rate (mm/hr) generated from the MS-DA system at (a) 08 UTC 13 June, and (b) 06 UTC June 14. The intense precipitation is associated with an MCS.

Figure 2. The large-scale (or grid-scale) pressure vertical velocity (a1-a4), T forcing (b1-b4), and q forcing (c1-c4). Columns display the large-scale forcing fields for each grid scale: (a) D300, (b) D200, (c) D100, and (d) D50. Note the change in color scale with grid size and that the x-axis is UTC time starting at 00 UTC 13 June.

Figure 3. Subgrid-scale dynamic components for the thermodynamic fields ($\overline{\nabla \cdot V'T'}$ in Eq. (1)) for domains D300, D200, D100, and D50 (a1-a4). Given are also the grid-scale horizontal advection ($-V \cdot \nabla \overline{T}$ in Eq. (3), b1-b4), and their sum (c1-c4). The label SS denotes subgrid-scale, and LS denotes large-scale (or grid-scale). Note the change in color scale with grid size and that the x-axis is UTC time starting at 00 UTC 13 June.

Figure 4. Subgrid-scale dynamic components for the moisture fields ($\overline{\nabla \cdot V'q'}$ in Eq. (2)) for domains D300, D200, D100, and D50 (a1-a4). Given are also the grid-scale horizontal advection ($-V \cdot \nabla \overline{q}$ in Eq. (4), b1-b4), and their sum (c1-c4). The label SS denotes subgrid-scale, and LS denotes large-scale (or grid-scale). Note the change in color scale with grid size and that the x-axis is UTC time starting at 00 UTC 13 June.

Figure 5. SCAM5-simulated precipitation rates for (a) D300, (b) D200, (c) D100, and (d) D50. There are four experiments for each grid scale: large/grid-scale forcing components

without a relaxation (LS_norelax, dashed blue), large/grid-scale forcing components with 3-hr relaxation (LS_3hrelax, dashed red), large/grid- plus subgrid-scale dynamic forcing components without a relaxation (LS+SS_norelax, solid blue), and large/grid- plus subgrid-scale dynamic forcing components with 3-hr relaxation (LS+SS_3hrelax, solid red). Given are also the domain-averaged surface precipitation rates from the ABRFC observations (black solid line) and from the MS-DA system (gray solid line). Note that the x-axis is UTC time starting at 00 UTC 13 June.

Figure 6. Time-height cross-section of cloud fractional occurrence from the ARMBE over the ARM SGP central facility. Note that the ARMBE is temporally averaged for a single geographical point and the x-axis is UTC time starting at 00 UTC 13 June.

Figure 7. SCAM5-simulated cloud fraction for D300 (a1 and b1), D200 (a2 and b2), D100 (a3 and b3), and D50 (a4 and b4). The simulations in the upper row (a1-a4) are driven with the large/grid-scale forcing, and the simulations in the lower row (b1-b4) are driven with the large/grid- plus sub-scale dynamic forcing components. No relaxation was applied. Note that the x-axis is UTC time starting at 00 UTC 13 June.

Figure 8. Same as Figure 7 but with 3-hr relaxation was applied. Note that the x-axis is UTC time starting at 00 UTC 13 June.

504

505

Table 1. SCAM5 Experiments. The forcing component for each experiment includes, by default, vertical advection of temperature and moisture. The following only highlights the differences between the experiments.

Experiment	Forcing component	Relaxation
LS_norelax	Grid-scale component only	No relaxation
LS_3hrelax	Grid-scale component only	3-hour relaxation
LS+SS_norelax	Grid-scale and subgrid-scale components	No relaxation
LS+SS_3hrelax	Grid-scale and subgrid-scale components	3-hour relaxation

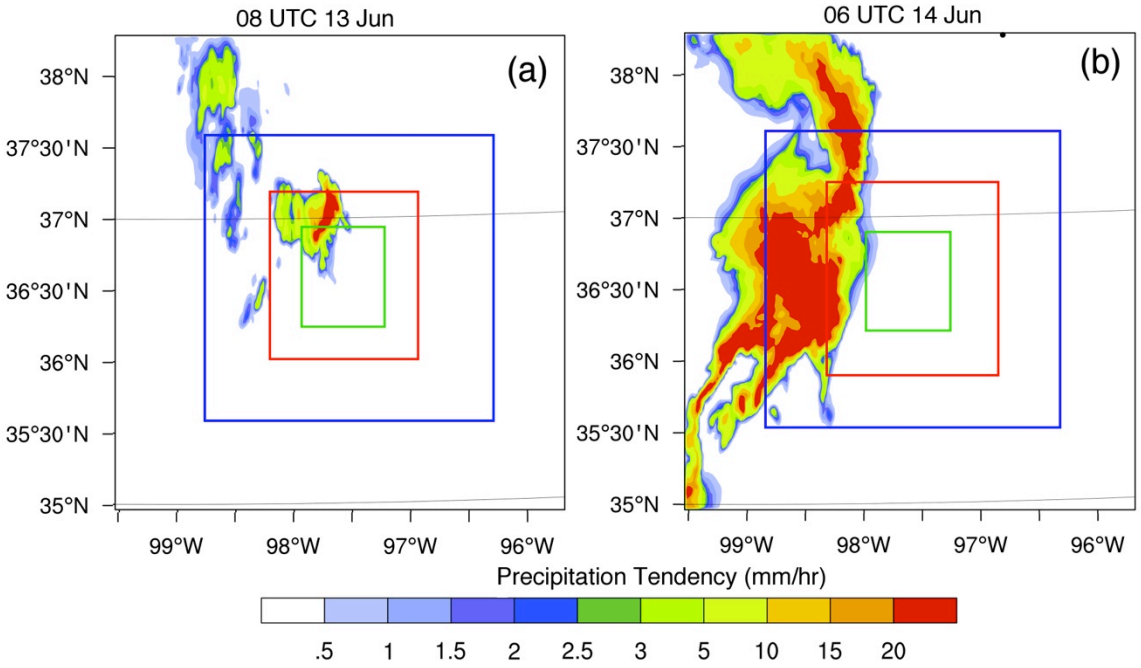

Figure 1. The domains used to calculate forcing components. The colored squares denote the following domains: 300 km × 300 km (black), 200 km × 200 km (blue), 100 km × 100 km (red), and 50 km × 50 km (green). All domains are centered on the ARM SGP central facility (36.63°N, 97.49°W). The color-filled contours show the distribution of surface precipitation rate (mm/hr) generated from the MS-DA system at (a) 08 UTC 13 June, and (b) 06 UTC June 14. The intense precipitation is associated with an MCS.

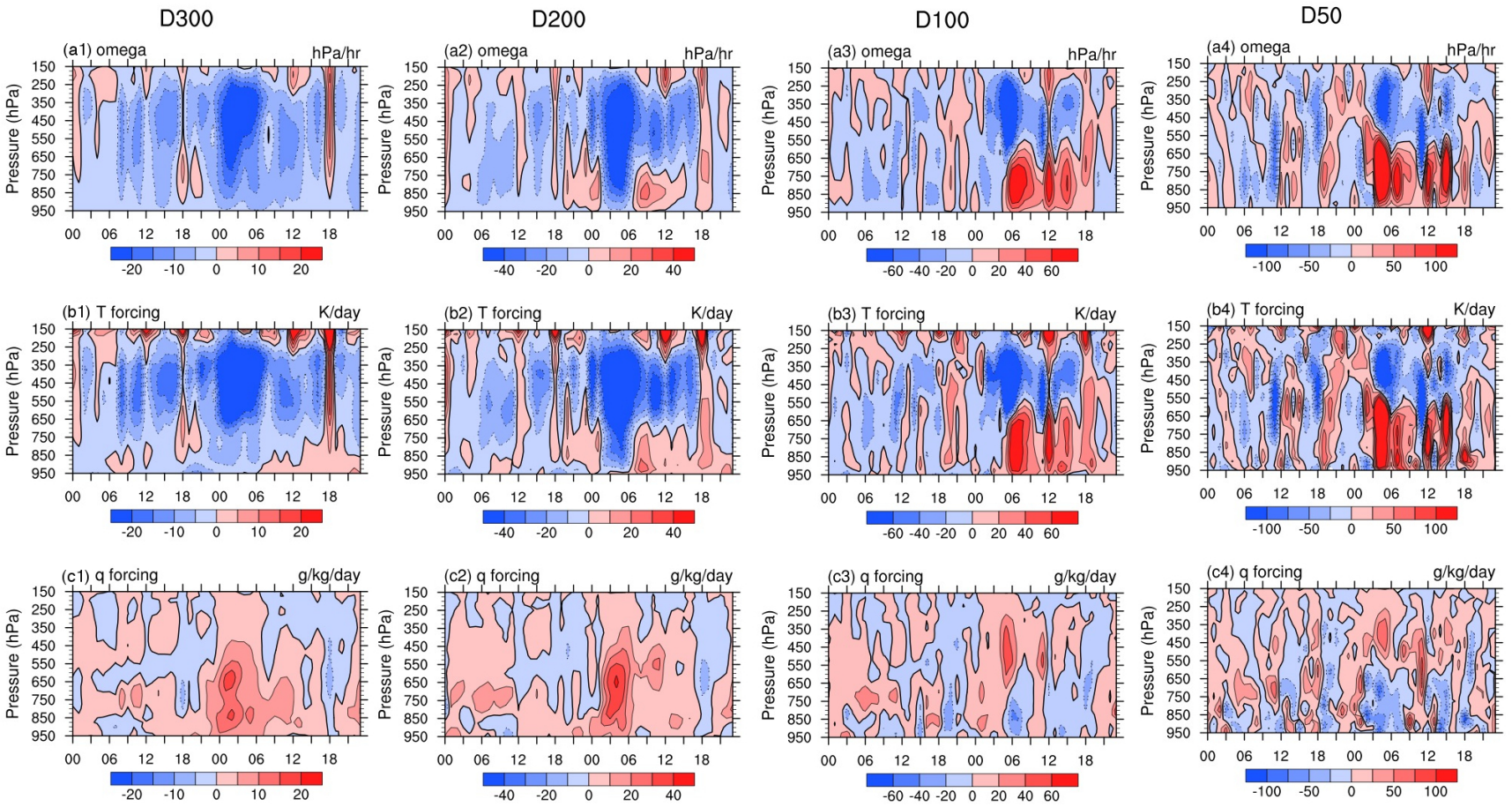

Figure 2. The large-scale (or grid-scale) pressure vertical velocity (a1-a4), T forcing (b1-b4), and q forcing (c1-c4). Columns display the large-scale forcing fields for each grid scale: (a) D300, (b) D200, (c) D100, and (d) D50. Note the change in color scale with grid size and that the x-axis is UTC time starting at 00 UTC 13 June.

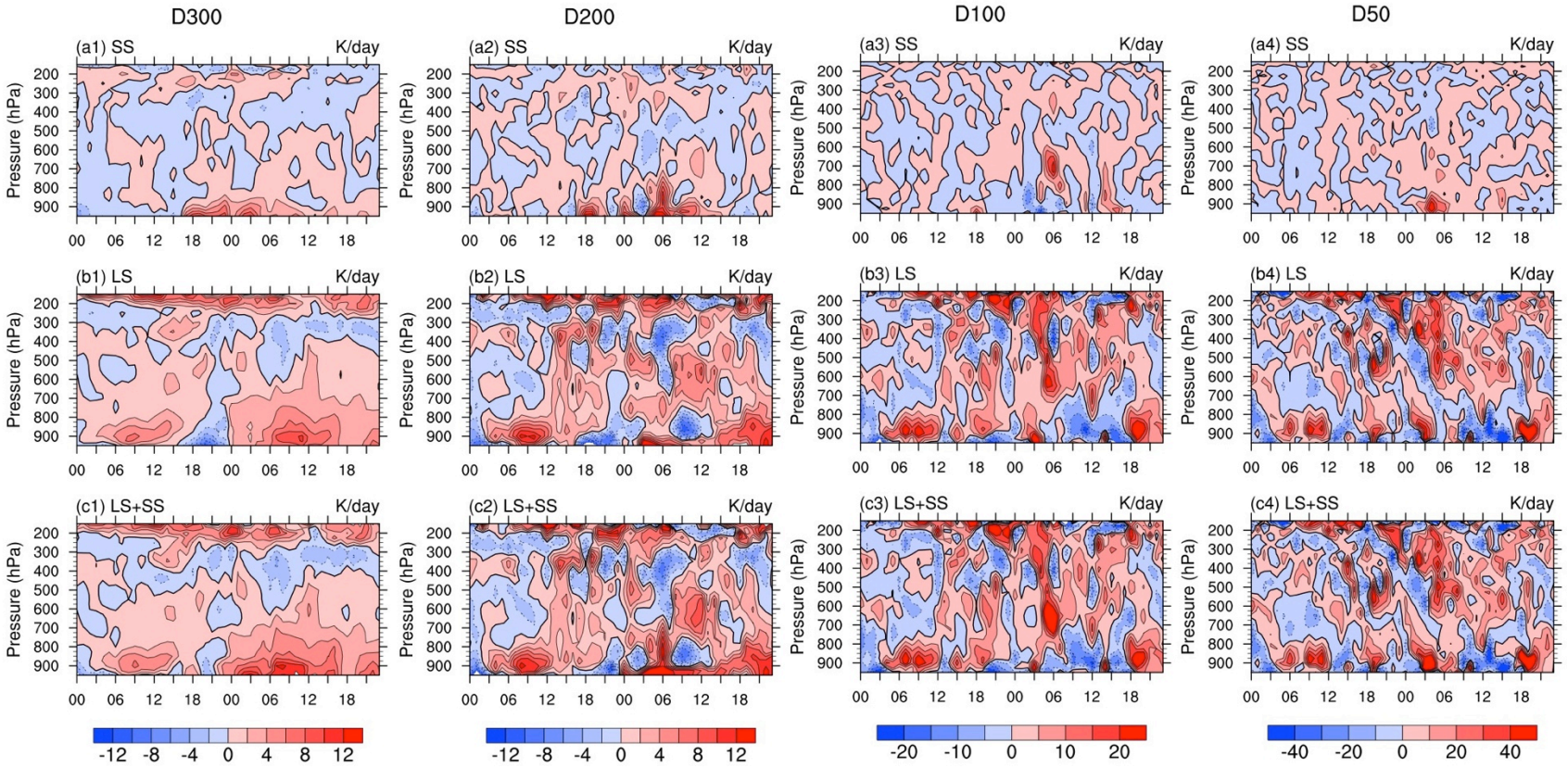

Figure 3. Subgrid-scale dynamic components for the thermodynamic fields ($\overline{\nabla \cdot V'T'}$ in Eq. (1), a1-a4) for D300, D200, D100, and D50 (a1-a4). Given are also the grid-scale horizontal advection ($-V \cdot \nabla \overline{T}$ in Eq. (3), b1-b4), and their sum (c1-c4). The label SS denotes subgrid-scale, and LS denotes large-scale (or grid-scale). Note the change in color scale with grid size and that the x-axis is UTC time starting at 00 UTC 13 June.

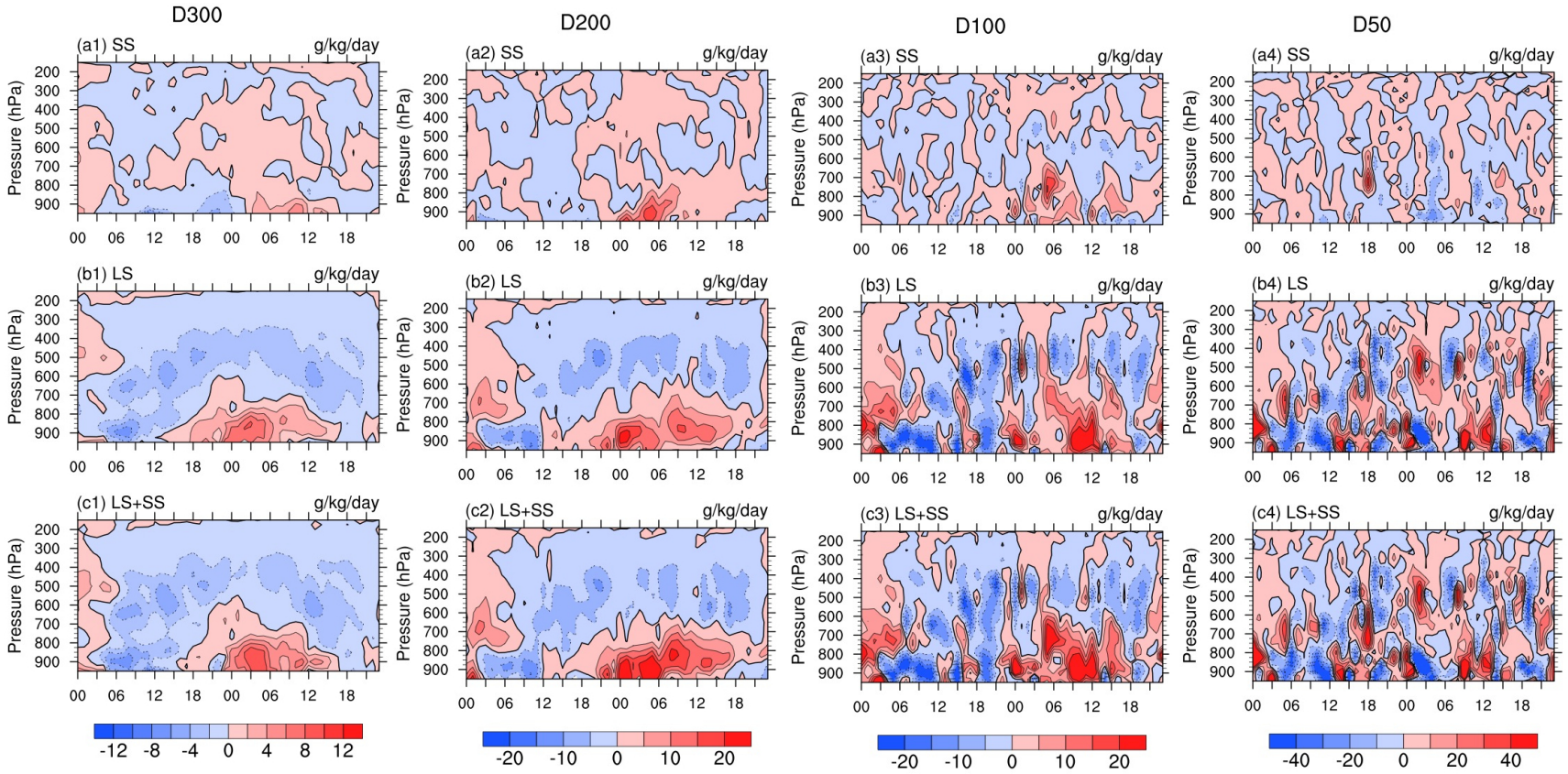

Figure 4. Subgrid-scale dynamic components for the moisture fields ($\overline{\nabla \cdot V'q'}$ in Eq. (2)) for domains D300, D200, D100, and D50 (a1-a4). Given are also the grid-scale horizontal advection ($-V \cdot \nabla \bar{q}$ in Eq. (4), b1-b4), and their sum (c1-c4). The label SS denotes

subgrid-scale, and LS denotes large-scale (or grid-scale). Note the change in color scale with grid size and that the x-axis is UTC time starting at 00 UTC 13 June. .

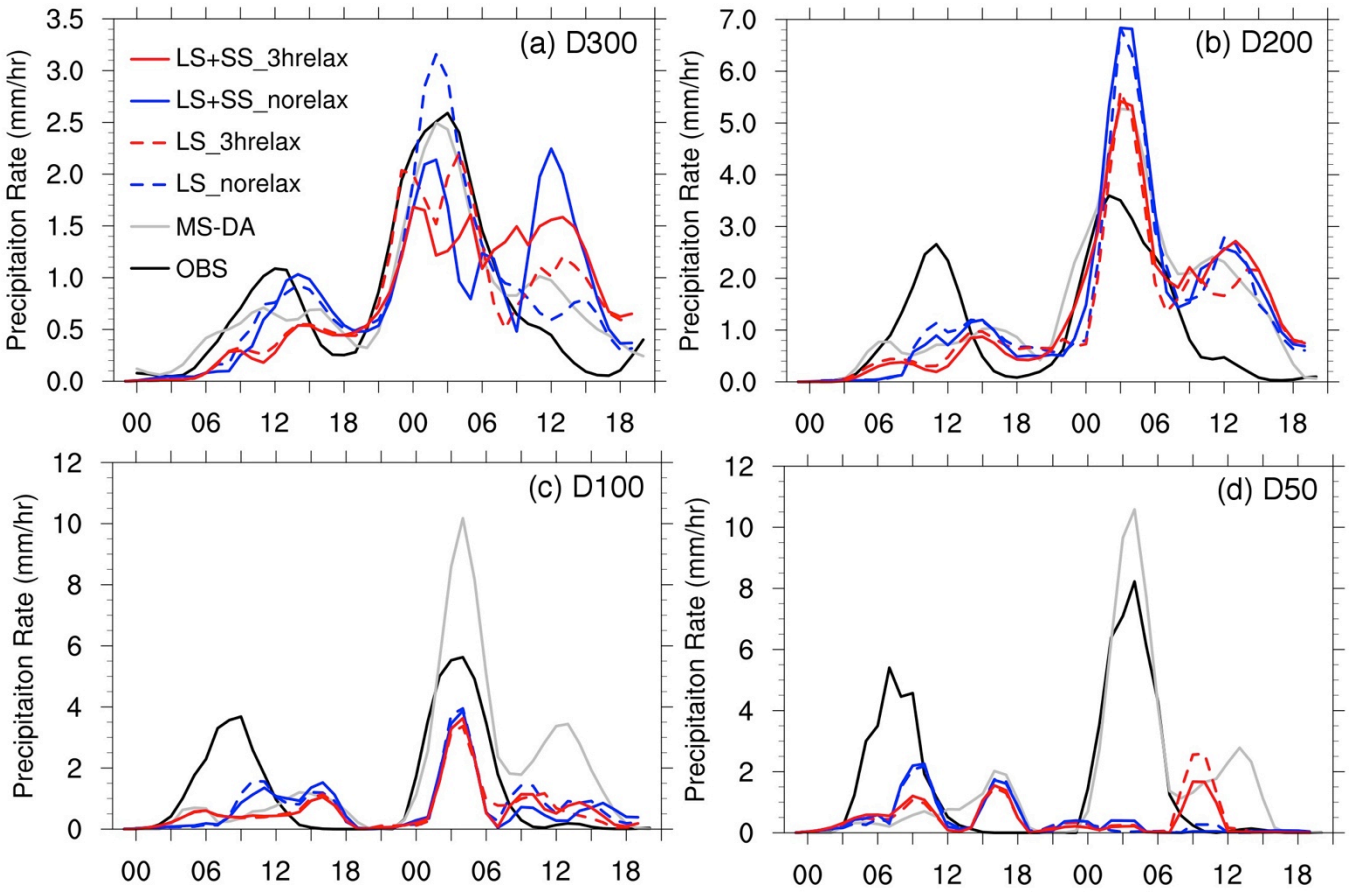

Figure 5. SCAM5-simulated precipitation rates for (a) D300, (b) D200, (c) D100, and (d) D50. There are four experiments for each grid scale: large/grid-scale forcing components without a relaxation (LS_norelax, dashed blue), large/grid-scale forcing components with 3-hr relaxation (LS_3hrelax, dashed red), large/grid- plus subgrid-scale dynamic forcing components without a relaxation (LS+SS_norelax, solid blue), and large/grid- plus subgrid-scale dynamic forcing components with 3-hr relaxation (LS+SS_3hrelax,

solid red). Given are also the domain-averaged surface precipitation rates from the ABRFC observations (black solid line) and from the MS-DA system (gray solid line). Note that the x-axis is UTC time starting at 00 UTC 13 June.

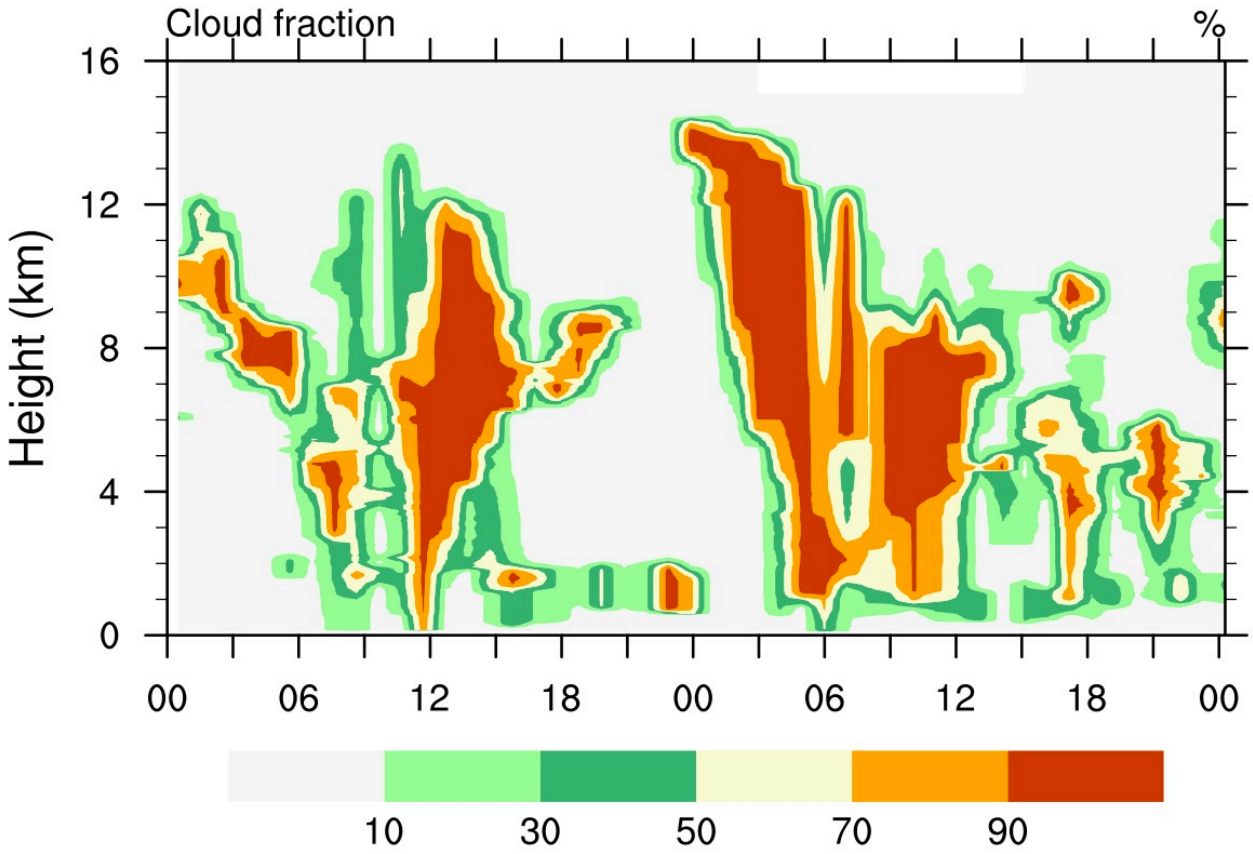

Figure 6. Time-height cross-section of cloud fractional occurrence from the ARMBE over the ARM SGP central facility. Note that the ARMBE is temporally averaged for a single geographical point and the x-axis is UTC time starting at 00 UTC 13 June.

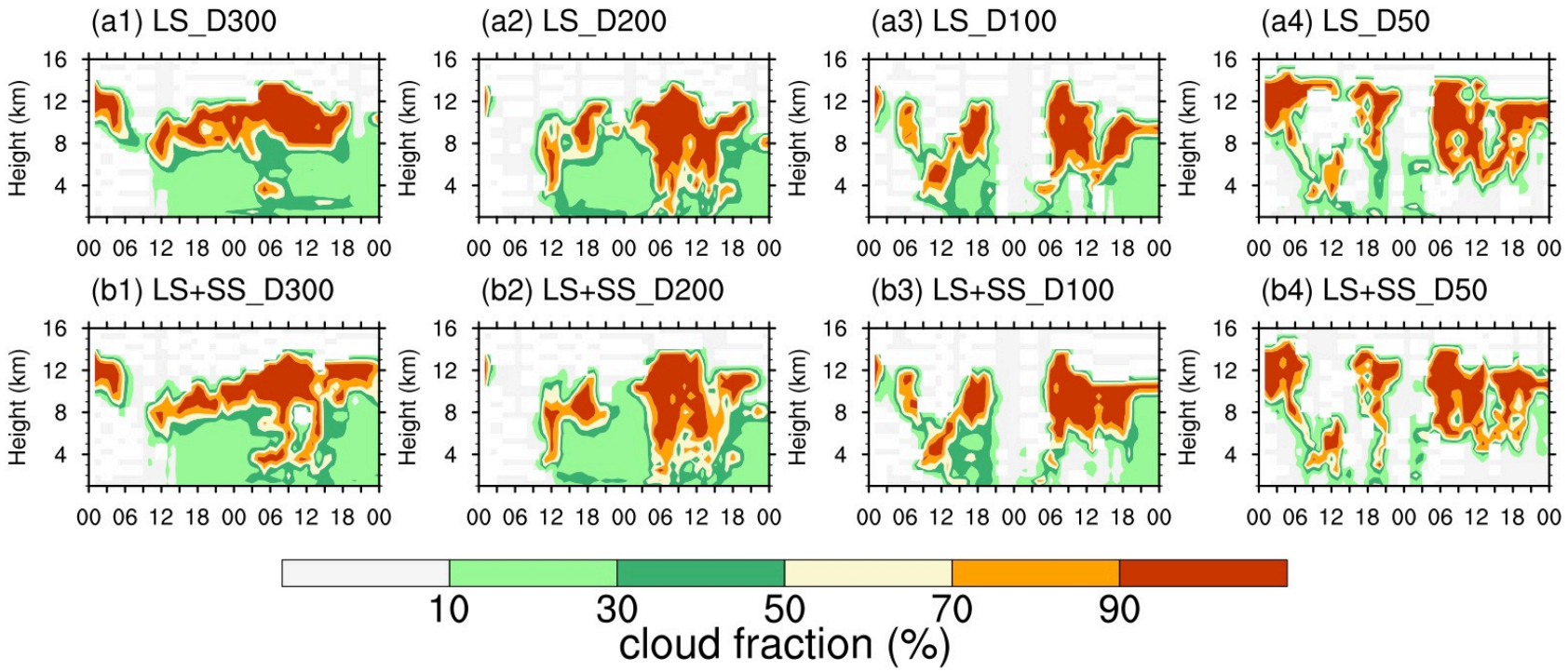

Figure 7. SCAM5-simulated cloud fraction for D300 (a1 and b1), D200 (a2 and b2), D100 (a3 and b3), and D50 (a4 and b4). The simulations in the upper row (a1-a4) are driven with the large/grid-scale forcing, and simulations in the the lower row (b1-b4) are driven with the large/grid- plus sub-scale dynamic forcing components. No relaxation was applied. Note that the x-axis is UTC time starting at 00 UTC 13 June.

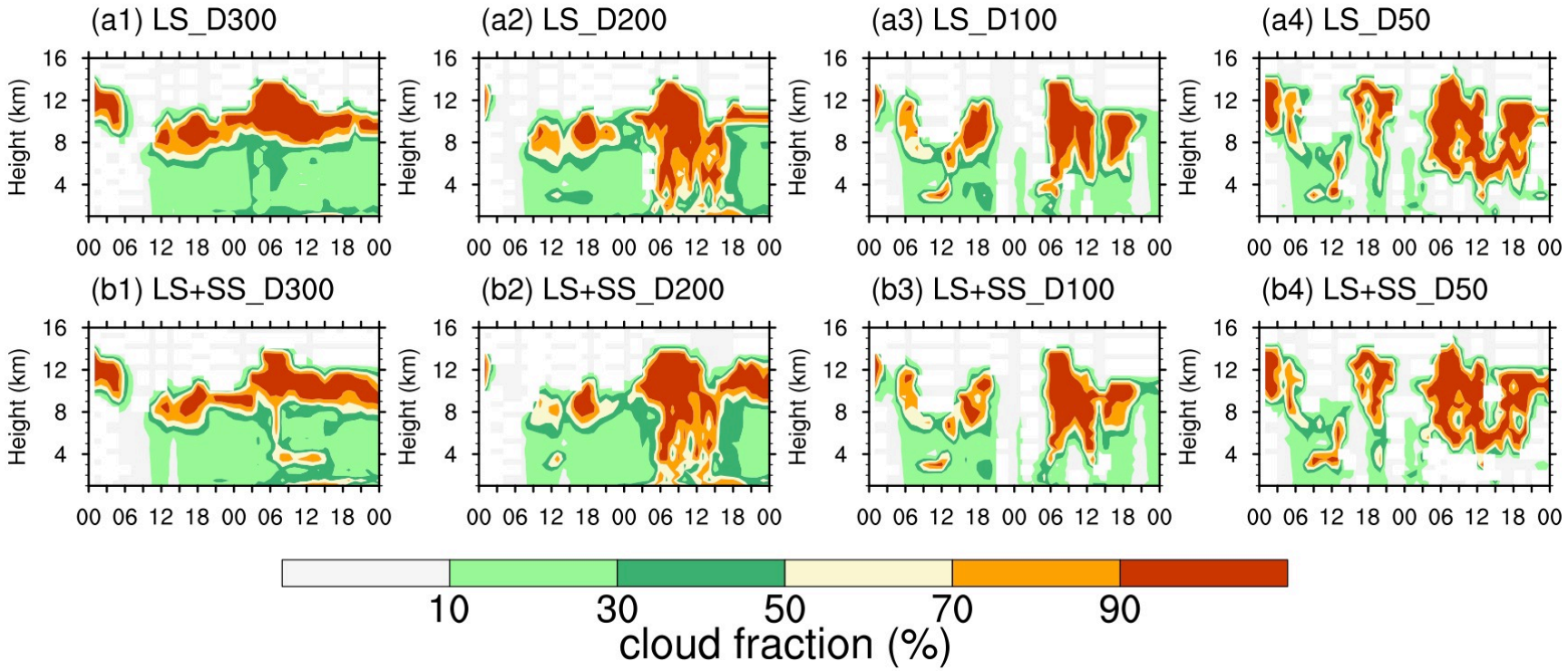

Figure 8. Same as Figure 7 but with 3-hr relaxation applied. Note that the x-axis is UTC time starting at 00 UTC 13 June.

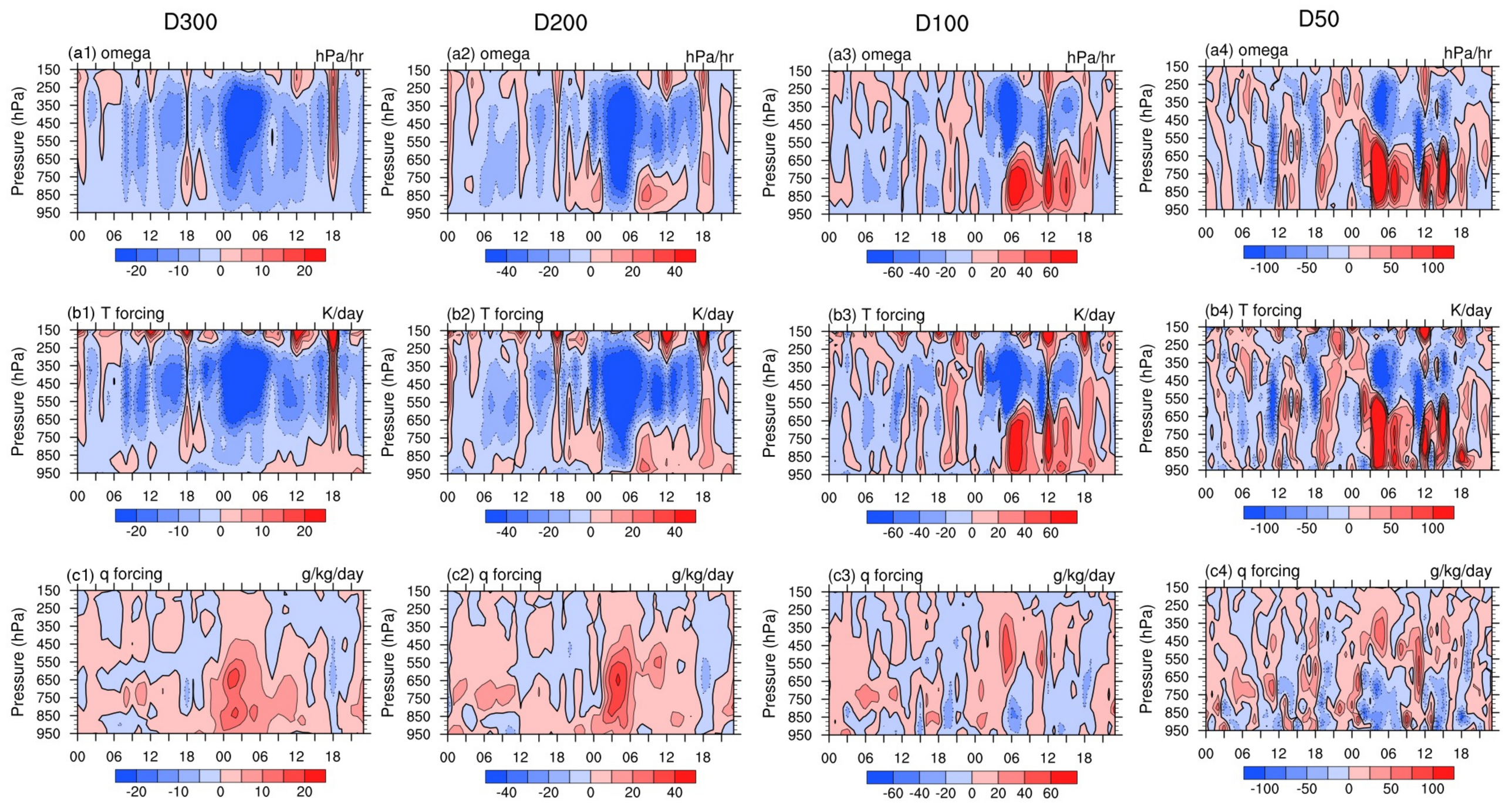
D300
D200
D100
D50
(a1) omega
hPa/hr
(a2) omega
hPa/hr
(a3) omega
hPa/hr
(a4) omega
hPa/hr
(b1) T forcing
K/day
(b2) T forcing
K/day
(b3) T forcing
K/day
(b4) T forcing
K/day
(c1) q forcing
g/kg/day
(c2) q forcing
g/kg/day
(c3) q forcing
g/kg/day
(c4) q forcing
g/kg/day
Pressure (hPa)
150
250
350
450
550
650
750
850
950
00 06 12 18 00 06 12 18
-20 -10 0 10 20
-40 -20 0 20 40
-60 -40 -20 0 20 40 60
-100 -50 0 50 100

08 UTC 13 Jun

06 UTC 14 Jun

(a)

(b)

38°N
37°30'N
37°N
36°30'N
36°N
35°30'N
35°N

99°W
98°W
97°W
96°W

Precipitation Tendency (mm/hr)

.5
1
1.5
2
2.5
3
5
10
15
20

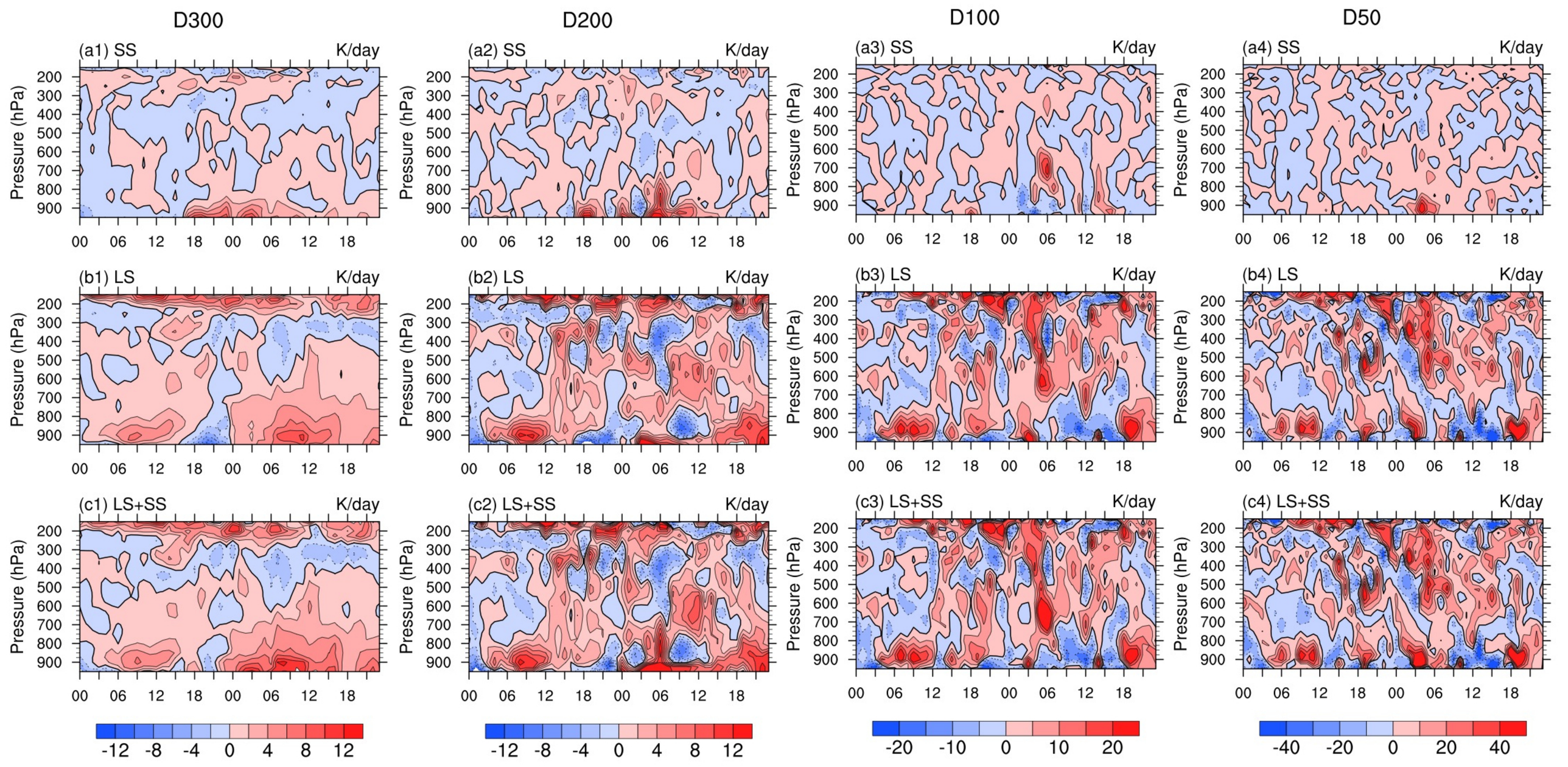
D300
D200
D100
D50
(a1) SS
(a2) SS
(a3) SS
(a4) SS
(b1) LS
(b2) LS
(b3) LS
(b4) LS
(c1) LS+SS
(c2) LS+SS
(c3) LS+SS
(c4) LS+SS
K/day
Pressure (hPa)
200
300
400
500
600
700
800
900
00
06
12
18
-12 -8 -4 0 4 8 12
-20 -10 0 10 20
-40 -20 0 20 40

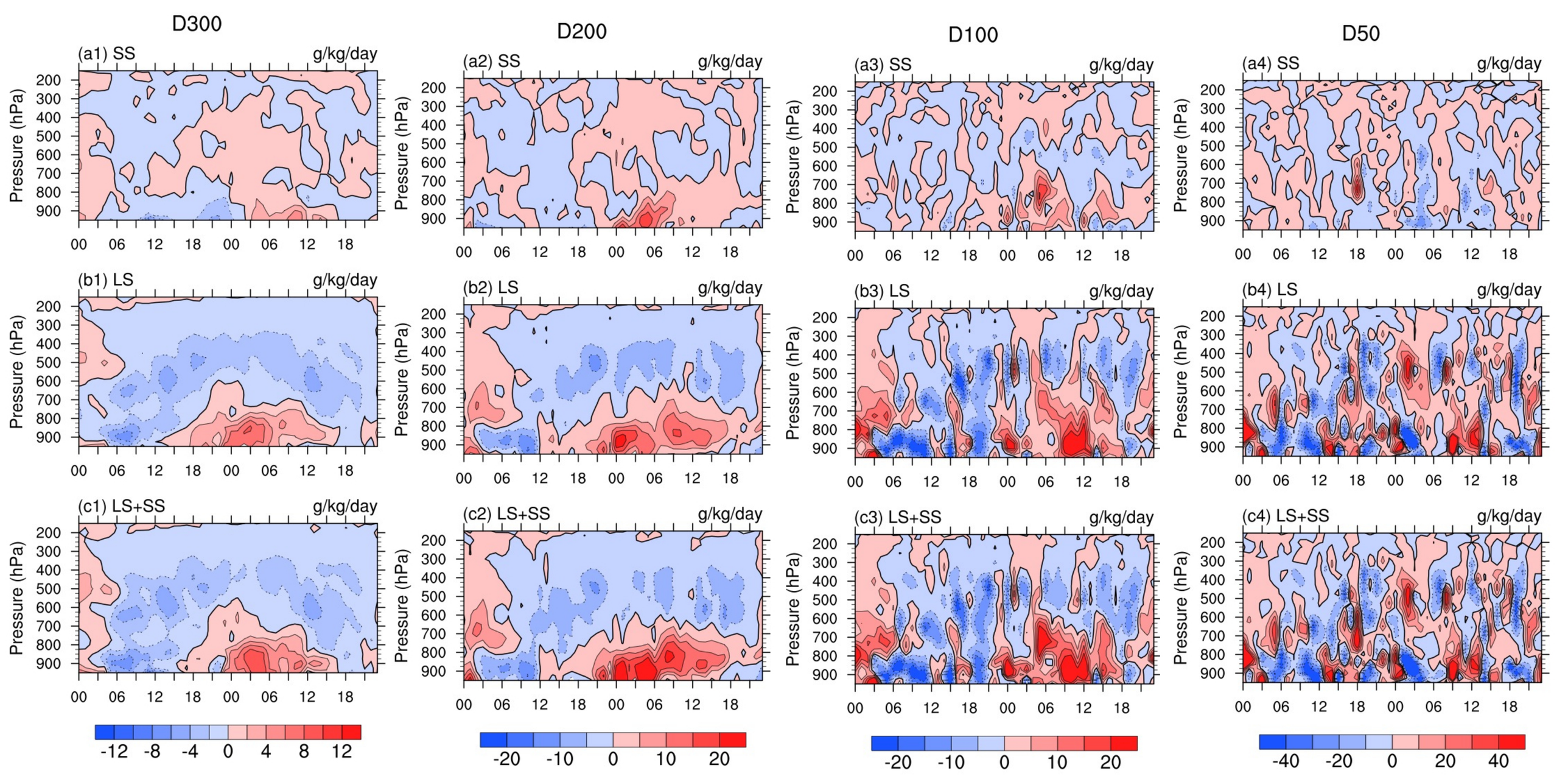
D300
D200
D100
D50
(a1) SS
(a2) SS
(a3) SS
(a4) SS
(b1) LS
(b2) LS
(b3) LS
(b4) LS
(c1) LS+SS
(c2) LS+SS
(c3) LS+SS
(c4) LS+SS
g/kg/day
Pressure (hPa)
200
300
400
500
600
700
800
900
00
06
12
18
-12 -8 -4 0 4 8 12
-20 -10 0 10 20
-20 -10 0 10 20
-40 -20 0 20 40

(a) D300

(b) D200

(c) D100

(d) D50

LS+SS_3hrelax
LS+SS_norelax
LS_3hrelax
LS_norelax
MS-DA
OBS

Precipitaiton Rate (mm/hr)

00 06 12 18 00 06 12 18

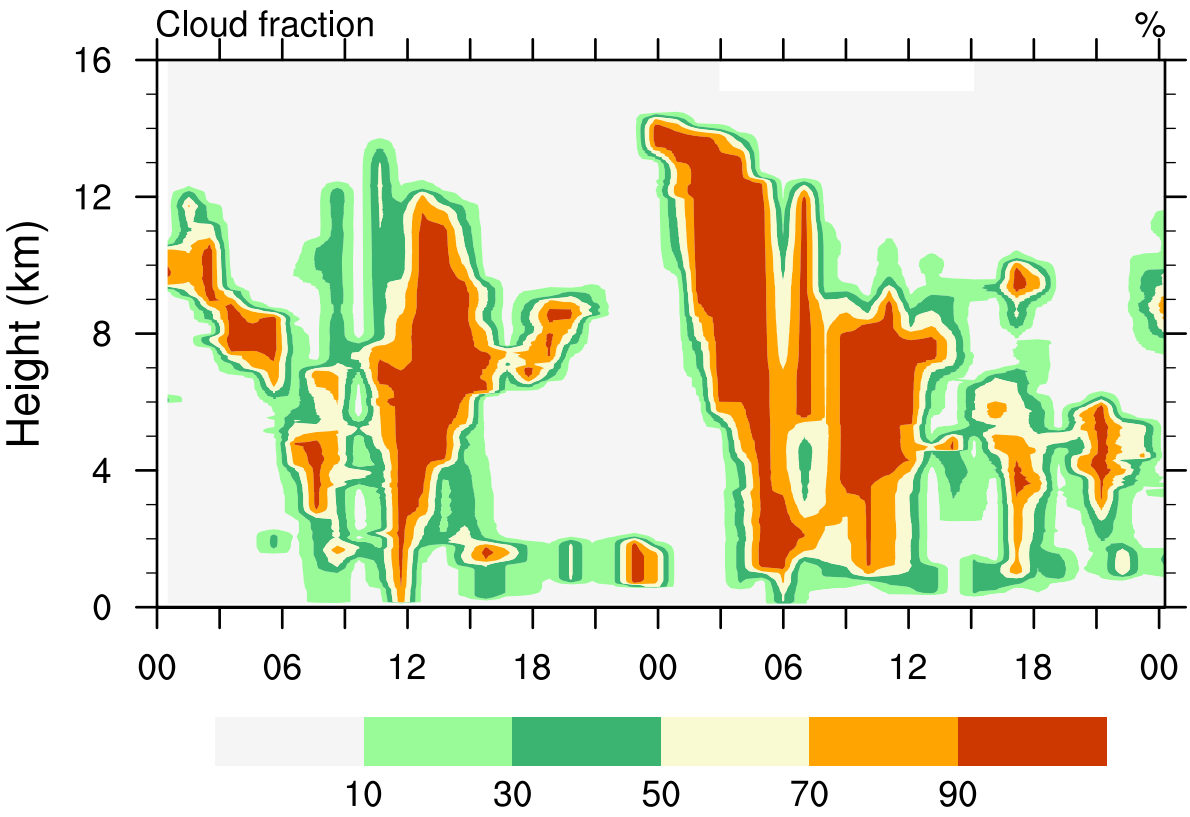
Cloud fraction
%
Height (km)
16
12
8
4
0
00
06
12
18
00
06
12
18
00
10
30
50
70
90

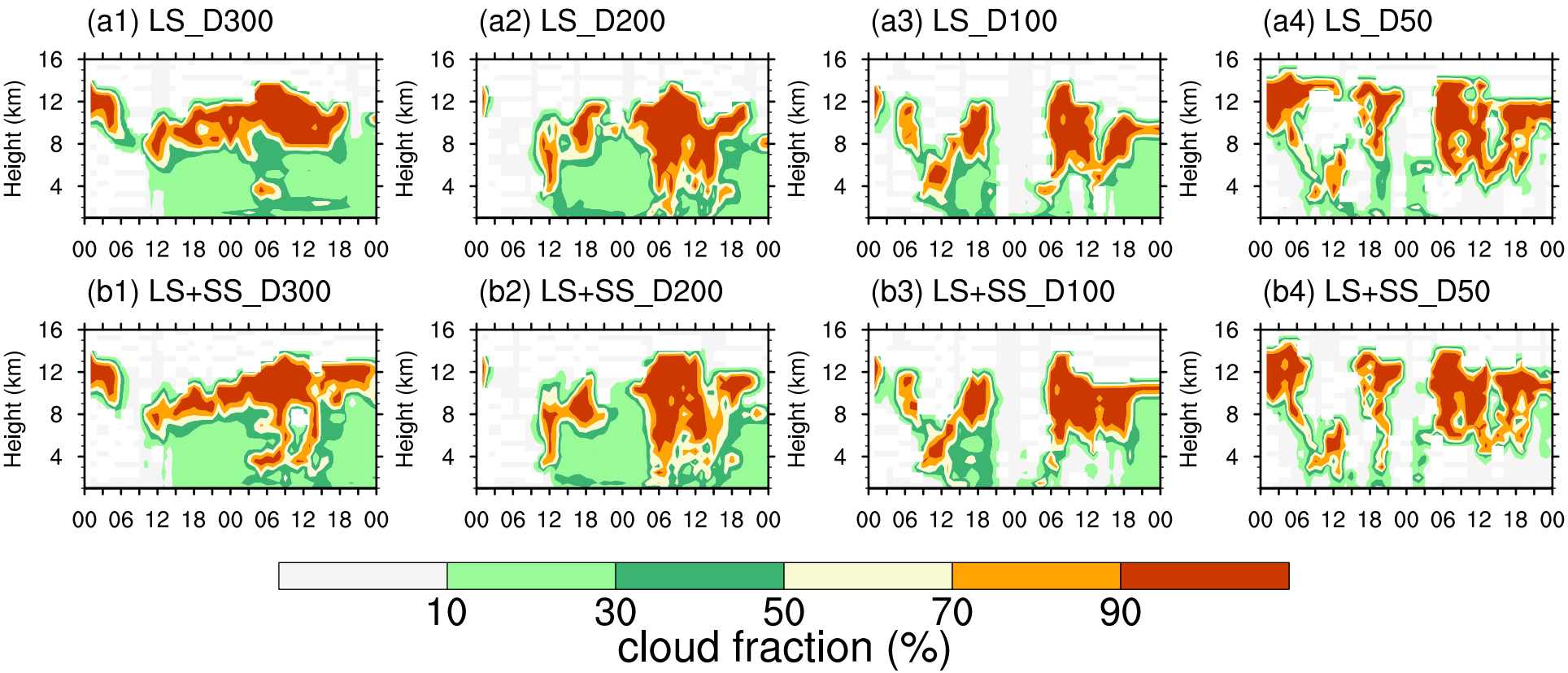
(a1) LS_D300
(a2) LS_D200
(a3) LS_D100
(a4) LS_D50
(b1) LS+SS_D300
(b2) LS+SS_D200
(b3) LS+SS_D100
(b4) LS+SS_D50
Height (km)
16
12
8
4
00 06 12 18 00 06 12 18 00
10
30
50
70
90
cloud fraction (%)

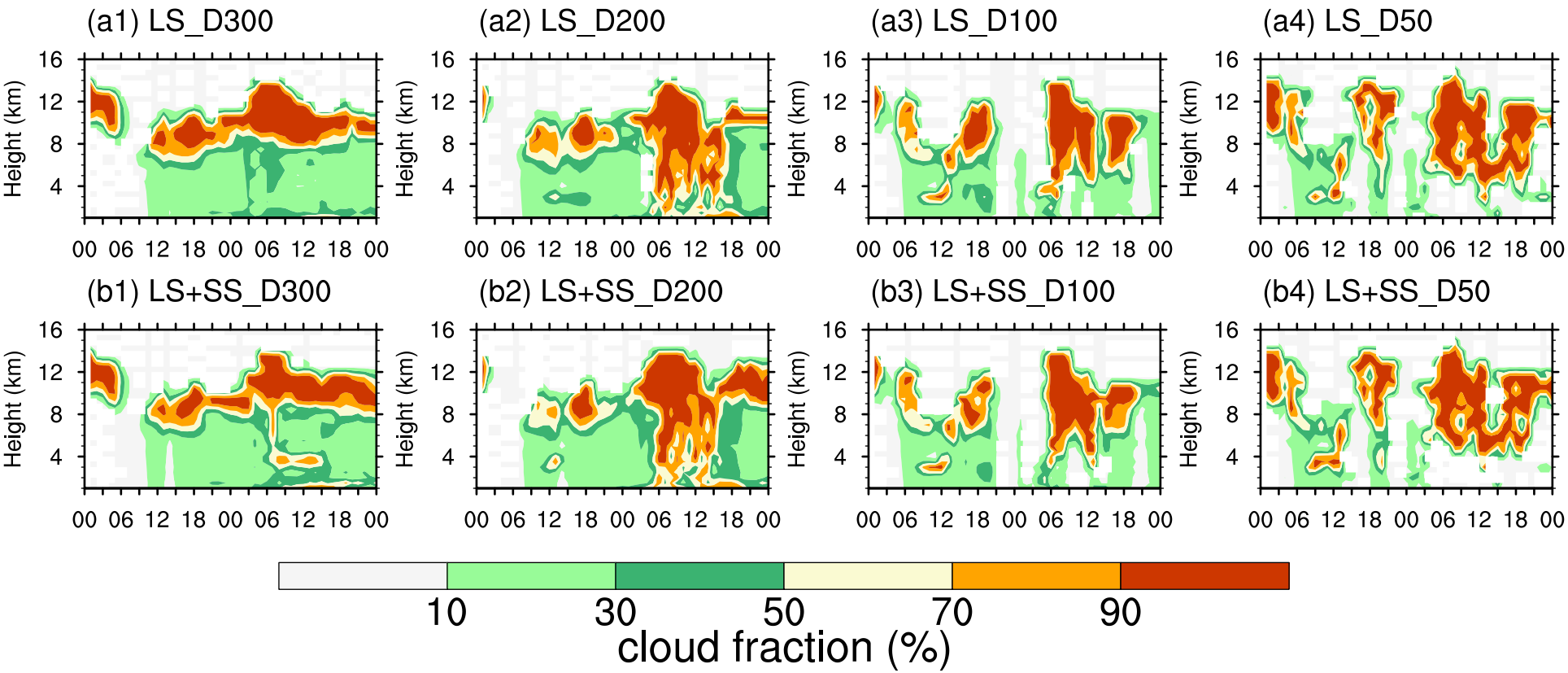
(a1) LS_D300
(a2) LS_D200
(a3) LS_D100
(a4) LS_D50
(b1) LS+SS_D300
(b2) LS+SS_D200
(b3) LS+SS_D100
(b4) LS+SS_D50
Height (km)
16
12
8
4
00 06 12 18 00 06 12 18 00
10
30
50
70
90
cloud fraction (%)